14th International Symposium on Turbulence and Shear Flow Phenomena (TSFP14)
Heidelberg, Germany, July 28–31, 2026

DECOUPLING THE EFFECTS OF PERMEABILITY AND ROUGHNESS

Dea D. Wangsawijaya[1], **Prateek Jaiswal**[2], **and Bharath Ganapathisubramani**[1]
[1] Aeronautical and Astronautical Engineering, University of Southampton
University Road, SO17 1BJ, United Kingdom
D.D.Wangsawijaya@soton.ac.uk
[2] Mechanical Engineering, University of Wisconsin-Madison
1500 Engineering Dr., Madison, WI 53706-1609, United States

ABSTRACT

A representation of a turbulent boundary layer (TBL) developing over a porous wall may include both "permeability" and "roughness" effects, to an extent. In this study, the possibility of decoupling the effects of roughness and permeability in the resulting turbulent structures above porous walls is explored, with the focus on the velocity–wall-pressure fluctuation coherence. Measurements are conducted over combinations of porous walls with a systematic variation of roughness effects. Present results suggest that the superposition of rough and permeable walls affects both small- and large-scale coherence between streamwise velocity u' and wall-pressure fluctuations p' across the TBL, although it does not seem to prominently affect the large-scale coherence in the outer layer. Near the wall, however, small-scale coherence is affected by the surface geometry. This behaviour seems to be Reynolds invariant across the range of Reynolds number *Re* tested in this study.

INTRODUCTION

A TBL developing over a porous wall comprises an extensive number of phenomena in nature and engineering applications. An example of the latter is the usage of a porous trailing edge to reduce airfoil noise up to a certain frequency (Carpio *et al.*, 2019), above which the roughness effect takes over the permeability effect (Geyer *et al.*, 2010). A realistic representation of a porous wall, in fact, involves solid substrates arranged in a particular manner, forming a part-solid, part-hollow wall. Thus, to an extent, a porous wall can be represented by *both* "permeability" (the inverse of substrate resistance to the flow) and "roughness" (due to blockage from the solid substrate and protrusions of this substrate above the wall). Thus, the effects of both permeability and roughness must be considered for the characterisation of a TBL over a porous wall.

In terms of aerodynamic penalty, both porous and rough walls result in momentum deficits from a canonical, smooth wall TBL, which can be written as a vertical shift ΔU^+ (Hama, 1954) in the log region from the smooth-wall TBL mean streamwise velocity profile U,

$$U^+ = \frac{1}{\kappa}\ln(y+d)^+ + B - \Delta U^+ \tag{1}$$

where the viscous-scaled $U^+ \equiv U/U_\tau$ and $(y+d)^+ \equiv (y+d)U_\tau/\nu$. Here, U_τ is the friction velocity, κ is the von Kàrmàn constant, y the wall-normal locations, d the zero-plane displacement, ν the kinematic viscosity, and B the log-law intercept. For rough walls in the "fully rough" regime, ΔU^+ is solely a function of a roughness lengthscale, the equivalent sandgrain roughness k_s (Nikuradse, 1933),

$$\Delta U^+ = \frac{1}{\kappa}k_s^+ + B - B_{FR} \tag{2}$$

where $k_s^+ \equiv k_s U_\tau/\nu$ and $B_{FR} = 8.5$. Compared to rough walls, the framework for drag characterisation is less established. It has been suggested by Manes *et al.* (2011) that the square-root of substrate permeability $\sqrt{K}$ (in m) is the relevant lengthscale for porous wall momentum deficit. Later, Esteban *et al.* (2022) explored the possibility of defining a porous wall lengthscale using the established framework for rough walls (equation 2), where the suggested lengthscale is a superposition of K and the blockage lengthscale of the porous substrate k_{s_b}. Taking this approach further, a recent study by the authors (Wangsawijaya *et al.*, 2023) systematically varied the roughness effect while maintaining constant K. The suggested lengthscale is a superposition of K, k_{s_b}, and the lengthscale of the protruding roughness elements: k_{s_r}, $k_s = Re_K k_{s_b} f(k_{s_r})$, where $Re_K \equiv \sqrt{K}U_\tau/\nu$. Two possible formulations of $f(k_{s_r})$ were tested with promising results: a linear relation $k_s = Re_K k_{s_b} C k_{s_r}$ and an area-weighted power-mean similar to that of Hutchins *et al.* (2023), $k_s = [(Re_K k_{s_b})^n + k_{s_r}^n]^{1/n}$, where C and n are constants.

While the above approach marks the first attempt towards decoupling the effects of permeability and roughness in porous-wall TBLs, it is limited to the mean quantity of the flow (i.e. the drag penalty). Therefore, in this study, we explore the possibility of decoupling the effects of roughness and permeability in the resulting turbulent structures above porous walls. Specifically, we focus on the velocity–wall-pressure fluctuations coupling (Gibeau & Ghaemi, 2021). Experiments are designed and performed over combinations of porous and rough walls, with systematic variation of roughness effect while maintaining constant permeability.

EXPERIMENTAL SET-UP

Measurements are conducted inside the test section of the closed return boundary layer wind tunnel (BLWT) at the University of Southampton. The test surfaces, illustrated in figure 1(a), are laid on the floor (bottom surface) of the BLWT. Five test surfaces are constructed for this study: porous wall ('**P**',

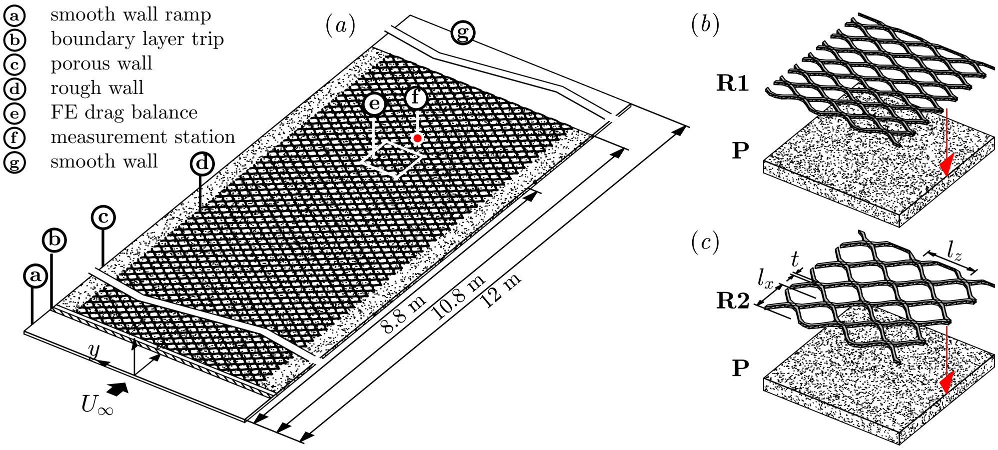

Figure 1. (a) Illustration of a test surface on the bottom floor of the test section of BLWT, measurement stations for direct wall-shear stress, hot-wire anemometry, and wall-pressure fluctuation measurements are marked by ⓔ and ⓕ. Combination of porous-rough test surfaces: (b) porous **P**–rough wall **R1**, and (c) porous **P**–rough wall **R2**. In (c), geometric parameters of the rough walls **R1** and **R2**: the width of mesh strands, $t = 4$ and 5 mm, streamwise width of the meshes, $l_x = 30$ and 53 mm, and spanwise width of the meshes, $l_z = 62$ and 70 mm, respectively. Adapted from Wangsawijaya *et al.* (2023).

Table 1. Summary of all test surfaces. The last column denotes symbols associated with test surfaces. Colours denote test cases with approximately matched Re_τ and $Re_K \approx$ 14400 and 13 (○), 18600 and 17 (○), 23400 and 20.5 (○), 27700 and 24 (○), 33100 and 27.5 (○).

Case	δ [mm]	θ [mm]	U_∞ [ms^{-1}]	U_τ [ms^{-1}]	Re_x [$\times 10^7$]	Re_θ [$\times 10^4$]	Re_τ [$\times 10^4$]	Re_K [–]	C_f [$\times 10^{-3}$]	ΔU^+ [–]	D^+ [–]	Sym.
						Porous walls						
P	201.11	24.55	19.84	1.06	1.18	3.29	1.44	13.62	5.72	12.01	455	○
	199.96	24.45	25.45	1.36	1.52	4.21	1.85	17.57	5.74	12.66	586	○
	208.26	25.37	29.06	1.54	1.76	5.07	2.21	20.22	5.65	13.02	675	○
	211.27	25.88	35.46	1.87	2.14	6.30	2.72	24.50	5.59	13.52	818	○
	221.25	26.43	40.05	2.13	2.39	7.18	3.20	27.52	5.67	13.81	919	○
						Rough walls						
R1	232.40	28.51	14.90	0.86	0.87	2.82	1.33	–	6.69	12.88	363	△
	236.84	28.78	19.93	1.15	1.17	3.83	1.82	–	6.70	13.64	489	△
	239.38	28.70	25.20	1.46	1.48	4.82	2.32	–	6.67	14.23	615	△
	243.78	28.84	29.58	1.71	1.73	5.68	2.77	–	6.69	14.65	723	△
	254.33	29.52	35.21	2.04	2.05	6.87	3.42	–	6.69	15.08	855	△
R2	241.11	29.41	15.10	0.89	0.89	2.96	1.44	–	7.01	13.44	378	◇
	229.33	28.56	19.74	1.18	1.15	3.75	1.79	–	7.09	14.14	496	◇
	229.34	28.25	24.90	1.49	1.46	4.68	2.27	–	7.12	14.74	628	◇
	230.03	28.64	29.83	1.78	1.75	5.69	2.73	–	7.13	15.21	754	◇
						Porous-rough walls						
PR1	225.41	26.90	17.28	1.06	1.01	3.08	1.58	13.32	7.48	14.08	444	☆
	218.12	27.17	21.47	1.31	1.26	3.90	1.92	16.74	7.49	14.66	559	☆
	227.93	27.28	26.04	1.60	1.54	4.78	2.46	20.55	7.60	15.19	686	☆
	226.64	27.33	31.49	1.94	1.85	5.74	2.94	24.65	7.60	15.65	823	☆
	229.11	27.28	35.01	2.17	2.05	6.36	3.31	27.46	7.67	15.93	916	☆
PR2	219.42	27.29	15.06	0.95	0.90	2.79	1.41	12.27	7.94	14.23	409	✡
	221.73	27.41	19.97	1.26	1.20	3.75	1.91	16.40	7.93	14.98	547	✡
	224.41	27.61	25.20	1.59	1.52	4.77	2.45	20.76	7.98	15.58	693	✡
	222.96	28.06	28.26	1.79	1.69	5.40	2.71	23.16	8.00	15.86	773	✡

figure 1(a)ⓒ), two types of rough walls ('**R1**' and '**R2**', figure 1b,c), and two combinations of rough walls on top of the porous wall ('**PR1**' and '**PR2**', figure 1b,c). A smooth wall ramp is installed at the datum (i.e., the inlet of the test section) to equalise the thickness of the test surfaces (figure 1(a)ⓐ), followed by a boundary-layer trip (figure 1(a)ⓑ) and the test surfaces (up to 10.8 m from the datum). The remaining downstream section of the floor ($10.8 \leq x \leq 12$ m) is covered by a smooth wall (figure 1(a)ⓖ).

Table 1 summarises all test cases, measured at 8.8 m from the datum (figure 1(a)ⓕ) at a range of freestream velocity U_∞. These cases correspond to two sets of approximately matched friction Reynolds numbers $Re_\tau \equiv \delta U_\tau/\nu \pm 1600$ (δ is the 99% boundary-layer thickness) and matched $Re_K \pm 10\%$. The first set is **P**, **R1**, and **PR1** (Re_τ and $Re_K \approx$ 14400 and 13, 18600 and 17, 23400 and 20.5, 27700 and 24, 33100 and 27.5), while the second set is **P**, **R2**, and **PR2** (4 cases up to Re_τ and $Re_K \approx$ 27700 and 24). In the last column of table 1, symbols denote test surfaces, while colours denote test cases with matched Re_τ and Re_K, which range from lighter to darker as Re_τ and Re_K increase.

Porous wall **P** is constructed from 15 mm-thick sheets of 45-ppi (pores per inch) polyurethane reticulated foam. The foam has a pore size of $s = 0.89$ mm, porosity (the ratio of empty-to-total volume) $\varepsilon = 0.97$, and permeability $K = 3.62 \times 10^{-8}$ m^2 (measured using a Darcy flow apparatus). The porosity is comparable to that of a sparse vegetation, $\varepsilon > 0.9$ (Luhar *et al.*, 2008), while the pore size ($s^+ \equiv sU_\tau/\nu \geq 63$) is comparable to the dense canopy of Sharma & García-Mayoral (2020), where $s^+ \approx 50$. The rough walls **R1** and **R2** are constructed from diamond-shaped, expanded metal mesh sheets illustrated in figure 1(b,c), respectively, with a smooth, solid wall below each sheet. **R1** is 3 mm-thick with an open area A_o (the ratio of empty-to-total area in xz–plane) of 0.73, while **R2** is 3.5 mm-thick with $A_o = 0.81$. The open-area lengthscales of the mesh sheets are $O(10^1)$ mm, two orders of magnitude larger than those of the porous wall (pore size is $O(10^{-1})$ mm). This ensures that the change in K is relatively negligible as the roughnesses are added on top of the porous wall.

Hot-wire anemometry (HWA) and wall-pressure fluctuation measurements are conducted simultaneously at a station marked by ⓕ in figure 1(a). A 5 μm-diameter, 1 mm-long portion of a tungsten wire (sensor lengths of $57 \leq l_w^+ \equiv l_w U_\tau/\nu \leq 145$) is soldered to the tip of a single-sensor, boundary-layer type probe and connected to a constant temperature anemometer. The instantaneous streamwise velocity component u is acquired across 35–40 logarithmically-spaced points in the y-direction from the wall towards the freestream, sampled at $f_s = 30$ kHz at each measurement point (corresponding to $t^+ \equiv U_\tau^2/(f_s \nu) \geq 1.6$). The sampling time T_s varies between test cases to ensure a boundary-layer turnover time of $T_s U_\infty/\delta > 20000$ for spectral convergence (Hutchins *et al.*, 2009). The sensor is calibrated before and after each measurement, with King's law defining the relationship between u and the output voltage of the sensor. A slight sensor drift is corrected by applying temperature compensation to the output signals.

The wall-pressure fluctuations p' are simultaneously acquired using a GRAS PH40 CCP free-field array microphone (diagphram diameter $D = 6.35$ mm, $363 \leq D^+ \equiv DU_\tau/\nu \leq 919$), with frequency response roll-off at ∼10 kHz, flush-mounted on the upper surface of the porous/solid walls, facing the open area of the mesh. The sensitivity of the microphone is 48.69 mV Pa^{-1}, measured using a GRAS 42AB sound calibrator (114 dB at 1 kHz). A different GRAS microphone of 34.43 mV Pa^{-1} sensitivity is used in **R1** and **R2** cases.

Finally, the dataset is completed with direct wall-shear stress measurements using an in-house drag balance (Aguiar Ferreira *et al.*, 2024) at a slightly upstream measurement station ($x = 8.6$ m, figure 1(a)ⓔ). The balance has a 20×20 mm floating element (FE), calibrated before the measurements using a set of calibration weights. A first-order polynomial defines the relationship between known weights and the output voltage, corresponding to a balance sensitivity of 93.15 mV g^{-1}.

FLOW STATISTICS

Figure 2(a) shows the skin friction coefficients $C_f \equiv 2(U_\tau/U_\infty)^2$ for all test cases as a function of fetch Reynolds numbers $Re_x \equiv xU_\infty/\nu$, directly measured by the drag balance. The measured C_f are first validated for baseline smooth-wall cases ('**SW**', $2390 \leq Re_\tau \leq 12500$) at the same measurement location (figure 1aⓔ) against the analytical solution of Monty *et al.* (2016) (solid black line in figure 2a). Results for the porous-rough test cases suggest that the rough walls **R1** and **R2** have higher C_f than the porous wall **P**, which further increases with the combination of both surfaces (**PR1** and **PR2**). All test cases (coloured open symbols in figure 2a) show that C_f is largely invariant to Re_x, suggesting that all cases fall into the "fully rough" regime. Thus, for rough walls, the skin friction drag is dominated by the form drag of the roughness elements, while for porous walls, it is the blockage of the porous substrate that dominates the friction drag. The momentum deficits due to porous-rough wall combinations are apparent in figure 2(b) as vertical downward shifts ΔU^+ from the inner-scaled mean streamwise velocity profile U^+ of case **SW**, shown for matched $Re_\tau \approx 27700$ cases. Here, ΔU^+ (reported in table 1) is obtained from a modified fitting method of Rodríguez-López *et al.* (2015), with U_τ directly measured by the drag balance, $\kappa = 0.39$ is maintained for all test cases, following the rough walls of Squire *et al.* (2016) and Gul & Ganapathisubramani (2021), and the fitted log-law intercept $B = 4.34 \pm 0.08$. Further, as shown in figure 2(c) for matched $Re_\tau \approx 27700$ cases, outer-layer similarity (OLS) is maintained for all test surfaces, as the velocity defect profiles collapse beyond $(y+d)/\delta \geq 0.2$ (dashed line in figure 2c). The OLS is also evident in the variance of the streamwise turbulent fluctuation in figure 2(d), shown in inner scale ($\overline{u'u'}^+ \equiv \overline{u'u'}/U_\tau^2$) as a function of y/δ for the same matched $Re_\tau \approx 27700$ cases. It should be noted, however, that the collapse in the variance profiles occurs later, approximately at $y/\delta \gtrsim 0.4$, compared to that of the mean profiles in figure 2(c).

Figures 3(a–c) show the power spectral density of p', $\Phi_{p'p'}$ as a function of resolved frequencies f for matched $Re_\tau \approx 27700$ and $Re_K \approx 24$ for all test surfaces (symbols correspond to different surfaces, see table 1). The data are presented in different scalings: $\Phi_{p'p'}/p_{ref}^2$ ($p_{ref} = 20$ μPa) as a function of f in Hz (figure 3a) and roughness-scaled f, fl_x/U_∞ (figure 3b), where l_x is the streamwise extent of the meshes parallel to the flow direction, as illustrated in figure 1(c), and outer-scaled $\Phi_{p'p'}U_\infty/(q^2\delta)$ as a function of $f\delta/U_\infty$ (figure 3c, q is the dynamic pressure of air). As shown in figure 3(a), compared to the rough walls **R1** and **R2**, porous wall reduces $\Phi_{p'p'}$ up to a certain frequency ($f \approx 1000$ Hz), above which $\Phi_{p'p'}$ rises above that of the rough walls, as the roughness effect takes over the permeability effect (Geyer *et al.*, 2010). Between the rough walls (dashed lines in figure 3a), **R1**, which has a smaller A_o (figure 1b), shows a reduction in $\Phi_{p'p'}$ up to $f \approx 200$ Hz compared to that of **R2**, above which $\Phi_{p'p'}$ of both

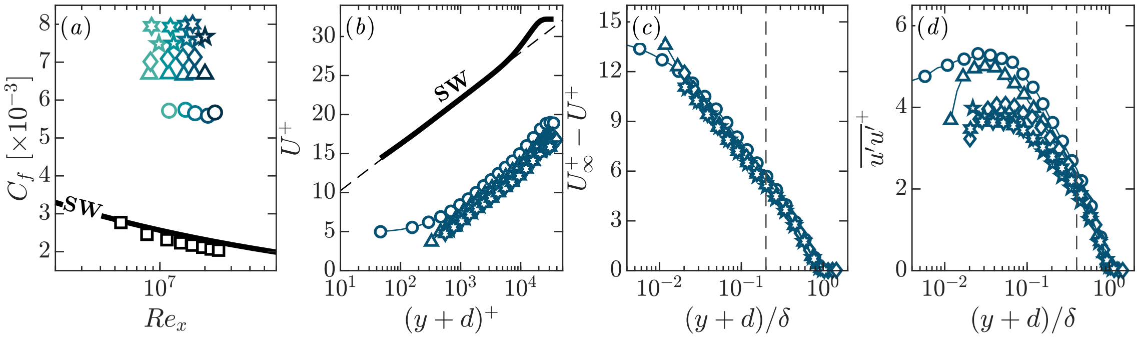

Figure 2. (a) C_f as a function of Re_x for all test surfaces. ━━: the analytical solution of Monty *et al.* (2016) for smooth wall TBLs (case '**SW**') and □: C_f of **SW** measured by a drag balance over a range of Re_x. (b) U^+ as a function of $(y+d)^+$ for all test surfaces at a matched $Re_\tau \approx 27700$ and $\Re_K \approx 24$. - - - : $1/\kappa \ln(y+d)^+ + B$. (c) Velocity defect $U^+_\infty - U^+$ as a function of $(y+d)/\delta$ at a matched $Re_\tau \approx 27700$. - - - : $(y+d)/\delta = 0.2$. (d) Viscous-scaled variance of streamwise velocity fluctuation $\overline{u'u'}^+$ as a function of $(y+d)/\delta$ a matched $Re_\tau \approx 27700$. - - - : $(y+d)/\delta = 0.4$. Legends are shown in table 1.

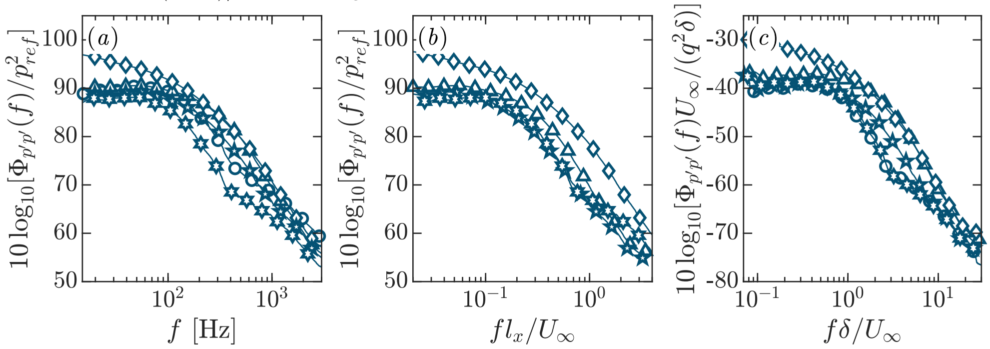

Figure 3. Power spectral density of wall-pressure fluctuations $\Phi_{p'p'}$ as a function of f at a matched $Re_\tau \approx 27700$ and $Re_K = 24$, shown (a) without normalisation, (b) in roughness scaling (l_x, figure 1c) and (c) in outer scaling. Legends are shown in table 1.

rough walls collapse. When combined, the effect of roughness and permeability superposition is evident. In figure 3(a), the magnitude $\Phi_{p'p'}$ of PR1 falls between that of **P** and **R1**, followed by a further reduction from that of **P** at $f \gtrsim 1000$ Hz. In contrast to **PR1**, **PR2** instead shows *further* $\Phi_{p'p'}$ reduction from that of **P** across all resolved frequencies. It is also observed in figure 3(b) that large-scale p' for cases **PR1** and **PR2** scales on the roughness lengthscales l_x up to $fl_x/U_\infty \approx 1$. When $\Phi_{p'p'}$ and f are presented in outer scales, figure 3c) shows that **P** and **R2** collapse in all resolved f (the effect of **R2** is not evident), while only large- and small-scales p' of **PR1** scales on δ.

ENERGY SPECTRA AND COHERENCE

Figures 4(a–e) show the contours of inner-scaled premultiplied energy spectra of streamwise turbulent fluctuations $f\Phi_{u'u'}/U^2_\tau$ for all test surfaces: **P**, **R1**, **R2**, **PR1**, **PR2**, respectively, at a matched $Re_\tau \approx 27700$ and $Re_K \approx 24$. The spectra are presented in viscous-scaled f and y in the lower abscissa and in the left-hand side ordinate, while the top abscissa and right-hand side ordinate show outer-scaled f and y, respectively. The porous wall spectra are characterised by "spectral shrinkage" (Jaiswal & Ganapathisubramani, 2024) over a frequency band ($0.3 \lesssim f\delta/U_\infty \lesssim 1$), shown as a dark purple region across the log and outer regions of the TBL in figure 4(a). By contrast, the shrinkage is not observed in rough walls **R1** and **R2** (figure 4b,c). While it is expected that the spectra of **PR1** and **PR2** will contain the footprints of both permeability and roughness, these are difficult to discern from figures 4(d,e). For this, another quantity, i.e. the coupling between u' and p', will be examined.

The turbulence–wall-pressure fluctuation coupling is analysed using the coherence between u' and p', defined as

$$C_{u'p'} = \frac{|\Phi_{u'p'}|^2}{\Phi_{u'u'}\Phi_{p'p'}} \tag{3}$$

where $\Phi_{u'p'}$ is the cross-spectra of u' and p'. Figures 4(f–j) show the contours of $C_{u'p'}$ for all test surfaces: **P**, **R1**, **R2**, **PR1**, **PR2**, respectively, at a matched $Re_\tau \approx 27700$ and $Re_K \approx 24$. While a higher magnitude of coherence is shown by both **R1** and **R2** at large-scale u' and p' across the TBLs (green to dark blue regions at $f\delta/U_\infty \approx 0.1$ in figure 4g,h), this region is concentrated in the log region $(y+d)^+ \lesssim 300$ at $f\delta/U_\infty \approx 1$ for porous wall (marked by '∘' in figure 4f). The footprints of porous and rough walls are evident in **PR1** and **PR2**, as the a higher magnitude of $C_{u'p'}$ is observed in two distinctive sites: small-scale u' and p' ($f\delta/U_\infty \approx 1$) in the log region ('∘' in figure 4i,j) and large-scale u' and p' ($f\delta/U_\infty \approx 0.2$) in the outer region of **PR1** and the log region of **PR2**, respectively (marked by '×' in figure 4i,j).

To decouple the effects of permeability and roughness, the coherence maps presented in figures 5(a–d) are $C_{u'p'}$ of **PR** cases subtracted by that of **P** and **R**. Figures 5(a,c) show $C_{u'p'}$ of cases **PR1** and **PR2** subtracted by that of **P**, respectively. The footprint of roughness is evident as the roughness elements break the near-wall structures: coherence decreases in the log region and below (blue-coloured contours in figure 5a) for case **R1** (smaller open area, figure 1b) and increases above $(y+d)/\delta \approx 0.2$ at $f\delta/U_\infty \approx 0.2$ ('×' in figure 5a). As the

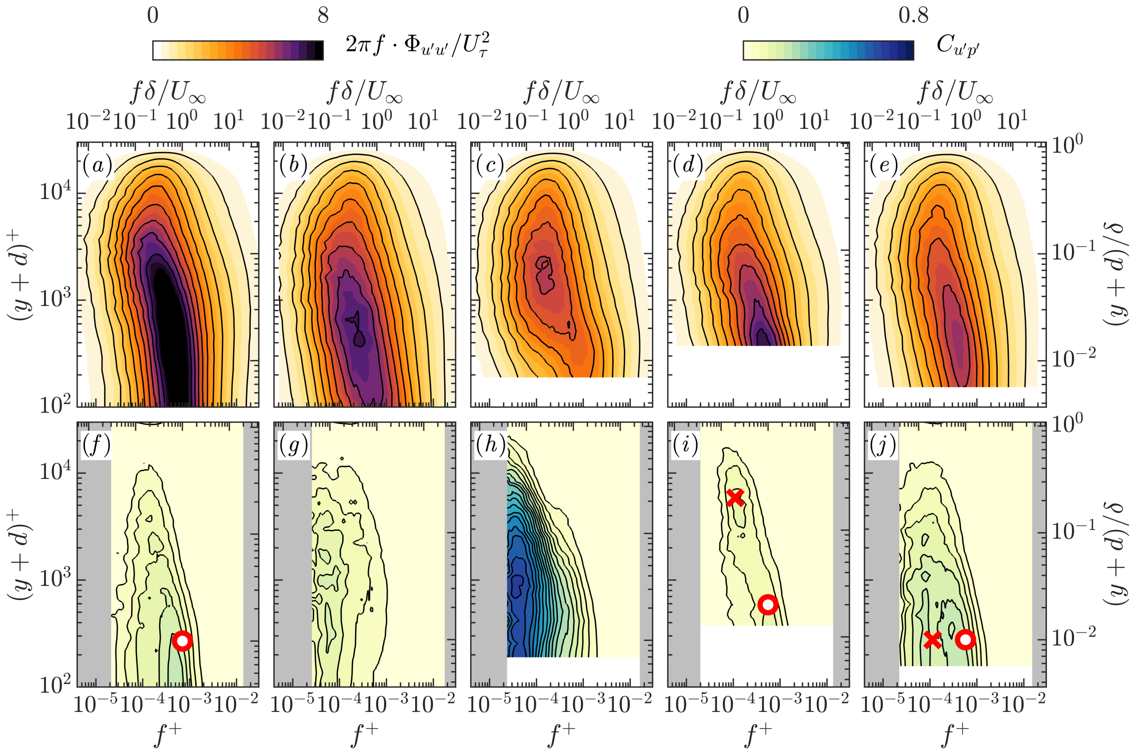

Figure 4. Coloured contours of premultiplied energy spectra of turbulent fluctuations, $f\Phi_{u'u'}$ as a function of f and y for cases: (a) **P**, (b) **R1**, (c) **R2**, (d) **PR1**, (e) **PR2** at a matched $Re_\tau \approx 27700$. Black contour lines are $2\pi f \cdot \Phi_{u'u'}/U_\tau^2 = 0.8, 1.6, \ldots, 8$. Coloured contours of u'–p' coherence $C_{u'p'}$ as a function of f and y for cases: (f) **P**, (g) **R1**, (h) **R2**, (i) **PR1**, (j) **PR2** at a matched $Re_\tau \approx 27700$. Black contour lines are $C_{u'p'} = 0.04, 0.08, \ldots, 0.8$. Grey-shaded areas in (f–j) mark the unresolved frequency bands. Inner- and outer-scaled f are presented on the bottom and top abscissas, while inner- and outer-scaled y are presented on the left- and right-hand side ordinates, respectively.

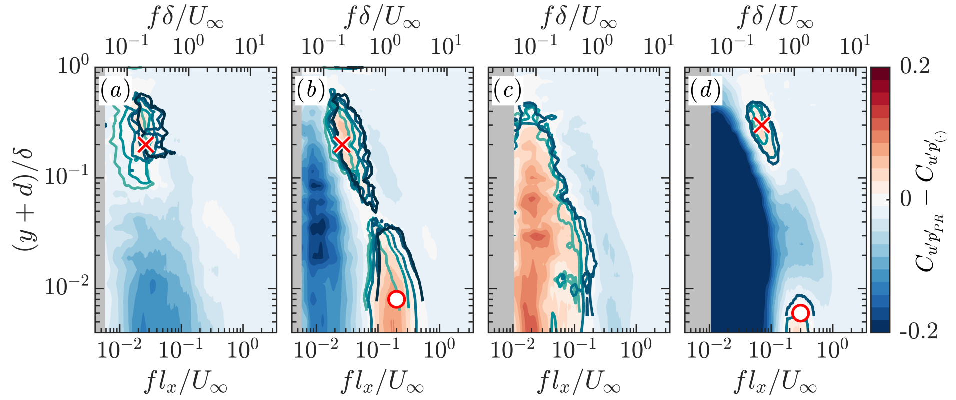

Figure 5. Coloured contours of $C_{u'p'}$ as a function of outer-scaled y and f of cases (a,b) **PR1** and (c,d) **PR2**, subtracted by $C_{u'p'}$ of (a,c) **P**, (b) **R1**, and (d) **R2** at a matched $Re_\tau \approx 27700$. Contour lines corresponds to $C_{u'p'_{\mathbf{PR}}} - C_{u'p'_{(\cdot)}} = 0.02$ for various Re_τ cases, with the same colour denoting matched Re_τ cases (see legends in table 1). Grey-shaded areas in (b,c,e,f) mark the unresolved frequency bands. l_x- and δ-scaled f are presented on the bottom and top abscissas.

mesh size increases in **R2** (figure 1c), the structures become more intact, as evidenced by a large-scale coherence across the TBL (red-coloured contours in figure 5c).

The addition of the porous wall under the mesh roughness, on the other hand, promotes entrainment of turbulent structures into the wall, as shown in the decreasing large-scale coherence across the TBL (blue-coloured contours in figures 5b,d). The smaller-scale coherence, however, increases for both **PR1** and **PR2** at two sites: closer to the wall ($(y+d)/\delta \lesssim 0.01$), which has a scale of $fl_x/U_\infty \approx 0.2$ (marked by '$\circ$' in figures 5b,d) and in the outer layer, with the scale of $f\delta/U_\infty 0.2$ (marked by '$\times$' in figures 5b,d). Taken together, the superposition of various rough and permeable walls does not seem to prominently affect the large-scale structures in the outer layer. Closer to the wall, however, the effect of surface geometry is evident: higher small-scale u'–p' coherence is observed at **PR1** ('o' in figure 5b) compared to **PR2** ('o' in figure 5d). This can be attributed to the breakdown of structures by the smaller open area mesh **R1** against structures grazing above the larger mesh **R2**. It should also be noted that this behaviour seems to be Reynolds invariant: the contour lines in figures 5(a–d), corresponding to the value of subtracted $C_{u'p'}$ of +0.02, largely remain on the same sites for all matched Re_τ and Re_K cases (from lighter to darker colours, see 1).

CONCLUSIONS

Simultaneous velocity–wall-pressure fluctuation measurements are conducted over combinations of porous walls with systematic roughness variations in an attempt to decouple the effect of permeability and roughness in the developing TBLs. Experiments are conducted over a set of matched Re_τ ($14400 \leq Re_\tau \leq 33100$) and Re_K ($13 \leq Re_K \leq 27.5$) for every porous-rough wall combination. Present results suggest that the superposition of various rough and permeable walls affects both small- and large-scale coherence between u' and p' across the TBL, although it does not seem to prominently affect the large-scale coherence in the outer layer. Near the wall, however, small-scale coherence is affected by the surface geometry, especially the mesh open area, which determines the breakdown and grazing of turbulent structures above the roughness elements. This behaviour seems to be consistent across the range of matched *Re* tested in this study.

REFERENCES

Aguiar Ferreira, M., Costa, P. & Ganapathisubramani, B. 2024 Wall shear stress measurement using a zero-displacement floating-element balance. *Exp. Fluids* **65**, 56.

Carpio, A. R., Martínez, R. M., Avallone, F., Ragni, D., Snellen, M. & van der Zwaag, S. 2019 Experimental characterization of the turbulent boundary layer over a porous trailing edge for noise abatement. *J. Sound Vib.* **443**, 537–558.

Esteban, L. B., Rodríguez-López, E., Ferreira, M. A. & Ganapathisubramani, B. 2022 Mean flow of turbulent boundary layers over porous substrates. *Phys. Rev. Fluids* **7** (9), 094603.

Geyer, T., Sarradj, E. & Fritzsche, C. 2010 Porous airfoils: noise reduction and boundary layer effects. *Int. J. Aeroacoustics* **9** (6), 787–820.

Gibeau, B. & Ghaemi, S. 2021 Low- and mid-frequency wall-pressure sources in a turbulent boundary layer. *J. Fluid Mech.* **918**, A18.

Gul, M. & Ganapathisubramani, B. 2021 Revisiting rough-wall turbulent boundary layers over sand-grain roughness. *J. Fluid Mech.* **911**, A26.

Hama, F. R. 1954 Boundary-layer characteristics for rough and smooth surfaces. *Trans. SNAME* **62**, 333–351.

Hutchins, N., Ganapathisubramani, B., Schultz, M. P. & Pullin, D. I. 2023 Defining an equivalent homogeneous roughness length for turbulent boundary layers developing over patchy or heterogeneous surface. *Ocean Eng.* **271**, 113454.

Hutchins, N., Nickels, T. B., Marusic, I. & Chong, M. S. 2009 Hot-wire spatial resolution issues in wall-bounded turbulence. *J. Fluid Mech.* **635**, 103–136.

Jaiswal, P. & Ganapathisubramani, B. 2024 Effects of porous substrates on the structure of turbulent boundary layers. *J. Fluid Mech.* **980**, A39.

Luhar, M., Rominger, J. & Nepf, H. 2008 Interaction between flow, transport and vegetation spatial structure. *Environ. Fluid Mech.* **8**, 423–439.

Manes, C., Poggi, D. & Ridolfi, L. 2011 Turbulent boundary layers over permeable walls: scaling and near-wall structure. *J. Fluid Mech.* **687**, 141–170.

Monty, J. P., Dogan, E., Hanson, R., Scardino, A. J., Ganapathisubramani, B. & Hutchins, N. 2016 An assessment of the ship drag penalty arising from light calcareous tubeworm fouling. *Biofouling* **32** (4), 451–464.

Nikuradse, J. 1933 Strömungsgesetze in rauhen rohren. *VDI Forschungsheft* **361**, English translation: 1950 Laws of flow in rough pipes. *NACA Tech. Mem.* **1292**.

Rodríguez-López, E., Bruce, P. J. K. & Buxton, O. R. H. 2015 A robust post-processing method to determine skin friction in turbulent boundary layers from the velocity profile. *Exp. Fluids* **56**, 68.

Sharma, A. & García-Mayoral, R. 2020 Turbulent flows over dense filament canopies. *J. Fluid Mech.* **888**, A2.

Squire, D. T., Morrill-Winter, C., Hutchins, N., Schultz, M. P., Klewicki, J. C. & Marusic, I. 2016 Comparison of turbulent boundary layers over smooth and rough surfaces up to high Reynolds numbers. *J. Fluid Mech.* **795**, 210–240.

Wangsawijaya, D. D., Jaiswal, P. & Ganapathisubramani, B. 2023 Towards decoupling the effects of permeability and roughness on turbulent boundary layers. *J. Fluid Mech.* **967**, R2.